Nonlinear Dynamics **7:** 451–470, 1995.

A Study of the Response of a Discontinuously Nonlinear Rotor System

D. H. GONSALVES, R. D. NEILSON and A. D. S. BARR
Department of Engineering, University of Aberdeen, Aberdeen, U.K.

(Received: 29 June 1993; accepted: 18 July 1994)

Abstract. In this paper the numerical and experimental response of a two degree of freedom, discontinuously nonlinear rotor system, which is subject to excitation by out-of-balance is considered. The nonlinearity in the form of a discontinuous stiffness is effected by a radial clearance between the elastically supported rotor and an elastically supported outer ring. The rotor is placed eccentrically within this ring so that it is just touching one side of the inner bearing housing.
The equations of motion for the system are presented and the numerical techniques used to solve them are described. A description of a corresponding experimental rig is presented, along with details of the procedures used to investigate its response.
By employing various chaos and spectral analysis techniques comparison is made between the results obtained from the two methods of investigation. Reasonable correlation is found. Subsequently, the results from further numerical simulations are presented which investigate the effect on the systems response when various system parameters are altered systematically. These show that the response of the system is extremely sensitive to changes in these parameters and that chaos can exist over large regions of the parameter space.

Key words: Rotordynamics, discontinuously nonlinear, clearance.

Notation

x	Displacement of rotor in horizontal direction
y	Displacement of rotor in vertical direction
M	Mass of the rotor
$m\rho$	Out of balance
Ω	Shaft speed
c	Damping coefficient
ν	Damping ratio
ν_2	Secondary damping ratio, associated with snubber ring
k_1	Primary (rotor support) stiffness
k_2	Secondary (snubber ring) stiffness
$\hat{K}$	Stiffness ratio, k_2/k_1
g	Radial clearance between rotor and snubber ring
ρ_1	$m\rho/M$
$\hat{\rho}_1$	Nondimensional ratio, ρ_1/g
ε	Eccentricity of rotor
$\hat{\varepsilon}$	Nondimensional ratio, ε/g
ω_n	Linear natural frequency, $\sqrt{k_1/M}$
$\hat{\Omega}$	Frequency ratio, Ω/ω_n

1. Introduction

Mechanical systems in which moving components contact intermittently with each other, such as impact oscillators, mechanical linkages, rotor systems with bearing clearances and gears are

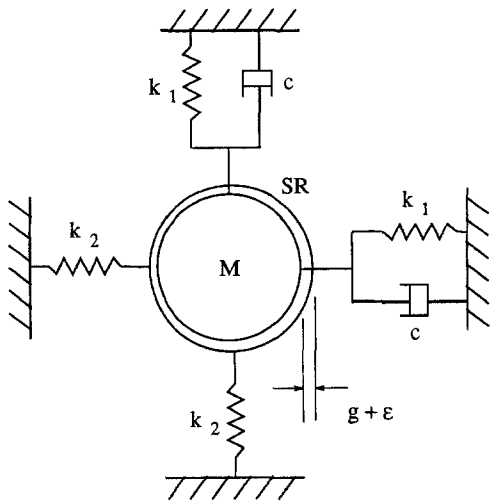

Fig. 1. Schematic representation of rotor system.

very common [1–5]. The presence of these clearances causes severe nonlinearities to occur, primarily in the form of discontinuous stiffness effects, which can lead to chaotic motions.

Rotor systems incorporating this type of nonlinearity have been studied in the past where the investigations concentrated mainly on periodic and aperiodic motions. More recently, though, the possibility of chaotic motion has been noted by Kim and Noah [6] in the response of a modified Jeffcott rotor system and by Ehrich [7] in the subcritical response of an eccentrically placed rotor. Work done by two of the authors [8, 9] centred on the numerical and experimental modelling of 4 and 6 degree of freedom rotor systems in which the likelihood of chaotic motions was inferred. However, due to the high dimensions of the phase space, the study of a simpler 2 degree of freedom system is undertaken here.

The aims of this work are two-fold. The first is to compare the response from an experimental rig with that from corresponding numerical simulations. The second is to show the sensitivity of the system to small changes in system parameters.

2. Description of Rotor Model

2.1. Equations of Motion

A schematic diagram of a rigid rotor system is provided in Figure 1. The radial clearance and the eccentricity of the rotor from the centre are denoted by g and ε, respectively. Hence, if the rotor is placed concentrically within the snubber ring, $\varepsilon = 0$.

When the rotor does not contact the ring, and measuring from the static equilibrium position of the shaft alone, depicted by the point O in Figure 2 the equation of motion in the x direction is

$$M\ddot{x} + c\dot{x} + k_1 x = m\Omega^2 \rho \cos \Omega t. \tag{1}$$

Similarly in the y direction the equation is

$$M\ddot{y} + c\dot{y} + k_1 y = m\Omega^2 \rho \sin \Omega t, \tag{2}$$

where the shaft rotation angle, Ωt is measured anti-clockwise from the direction of the x-axis.

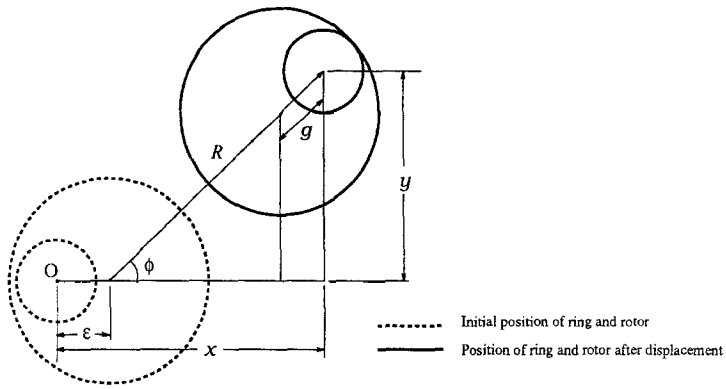

Fig. 2. Geometrical representation of rotor system.

When the displacements are large enough for the rotor to make contact with the snubber ring the secondary stiffness term, k_2 has to be included in the equations of motion, which now become nonlinear.

In the x direction the equation is

$$M\ddot{x} + c\dot{x} + k_1 x + k_2((R-g)\cos\phi) = m\Omega^2\rho\cos\Omega t \tag{3}$$

and in the y direction

$$M\ddot{y} + c\dot{y} + k_1 y + k_2((R-g)\sin\phi) = m\Omega^2\rho\sin\Omega t, \tag{4}$$

where

$$R = \sqrt{(x-\varepsilon)^2 + y^2}\,, \quad \cos\phi = \frac{x-\varepsilon}{R}\,, \quad \sin\phi = \frac{y}{R}\,,$$

and where $(R-g)$ is the radial motion of the outer ring relative to its initial position.

The above equations were derived having made certain assumptions, which include assuming that the dry friction between the ring and rotor was negligible and that the snubber ring was massless and hence could be simplified to having only a stiffness associated with it. The equations did not take into account the damping effect of the ring on the system either.

The equations were transformed into first order differential equations, which were then used for the computational modelling of the system.

2.2. Nondimensionalized Equations

The equations of motion were nondimensionalized [10] in order to derive the dimensionless parameters that govern the behaviour of the rotor system.

The time t is made dimensionless by using the rotor system's linear natural frequency, ω_n and displacements are nondimensionalized by using the radial clearance, g as the reference displacement. Let

$$\hat{t} = \omega_n t, \quad \hat{\Omega} = \frac{\Omega}{\omega_n}\,, \hat{\Omega}_2 = \frac{\Omega_2}{\omega_n} = \sqrt{\frac{k_2}{k_1}} = \sqrt{\hat{K}}\,, \quad \nu = \frac{c}{2\sqrt{k_1 M}}\,,$$

$$\rho_1 = \frac{m\rho}{M}\,, \quad \hat{x} = \frac{x}{g}\,, \quad \hat{y} = \frac{y}{g}\,, \quad \hat{\varepsilon} = \frac{\varepsilon}{g}\,, \quad \hat{\rho}_1 = \frac{\rho_1}{g}\,.$$

In terms of the above dimensionless quantities, R in the previous equations becomes

$$R = g\sqrt{(\hat{x} - \hat{\varepsilon})^2 + \hat{y}^2} = g\hat{z}.$$

Hence equation (3), for motion of the rotor in the x direction reduces to

$$\frac{d^2\hat{x}}{d\hat{t}^2} + 2\nu\frac{d\hat{x}}{d\hat{t}} + \hat{x} + \hat{K}\left((\hat{x} - \hat{\varepsilon})\left(1 - \frac{1}{\hat{z}}\right)\right) = \hat{\rho}_1\hat{\Omega}^2\cos\hat{\Omega}\hat{t}$$

and equation (4), for motion in the y direction becomes

$$\frac{d^2\hat{y}}{d\hat{t}^2} + 2\nu\frac{d\hat{y}}{d\hat{t}} + \hat{y} + \hat{K}\left((\hat{y}\left(1 - \frac{1}{\hat{z}}\right)\right) = \hat{\rho}_1\hat{\Omega}^2\sin\hat{\Omega}\hat{t}.$$

Thus, the motion of the rotor depends on the dimensionless parameters:

- $\hat{\Omega}$, the forcing to linear natural frequency ratio
- $\hat{K}$, the stiffness ratio, k_2/k_1
- ν, the damping ratio
- $\hat{\varepsilon}$, the eccentricity of the rotor from the centre to radial clearance ratio
- $\hat{\rho}_1$, the ratio of the imbalance level to radial clearance.

2.3. Discontinuity Functions

Due to the discontinuous (piecewise) nature of the equations of motion, the equations were solved numerically using a method developed by Borthwick [11], based on the fourth order Runge–Kutta algorithm, and modified by Neilson [12, 13] to include various algorithms to allow the detection of discontinuities and interpolation at the points of discontinuity. Discontinuity functions were formulated to detect in which range the rotor lay and consequently which set of equations should be solved in the numerical simulations. The functions are set to have a value of zero when the rotor just contacts the ring, negative when out of contact and positive when in contact. The displacement discontinuity function, δ is given by

$$\delta = R - g = \sqrt{(x - \varepsilon)^2 + y^2} - g. \tag{5}$$

The derivative of this function is therefore

$$\frac{d\delta}{dt} = \frac{x - \varepsilon}{R}\dot{x} + \frac{y}{R}\dot{y}. \tag{6}$$

Equations (5) and (6) were used to detect the points of discontinuity as described in [13].

Although methods other than numerical ones can be used, e.g., harmonic balance [6], these generally permit periodic solutions to be sought, excluding both quasi-periodic and chaotic solutions. Responses for these types of motion still need to be solved numerically. In addition, numerical simulation was the most convenient and consistent method for obtaining bifurcation diagrams to show regions of interest.

3. Description of Experimental Rotor System

The rotor system comprised essentially two main parts, a rigid rotor which was elastically supported by four flexural rods and excited by an out-of-balance mass and a snubber ring, which was also elastically supporting using four compression springs.

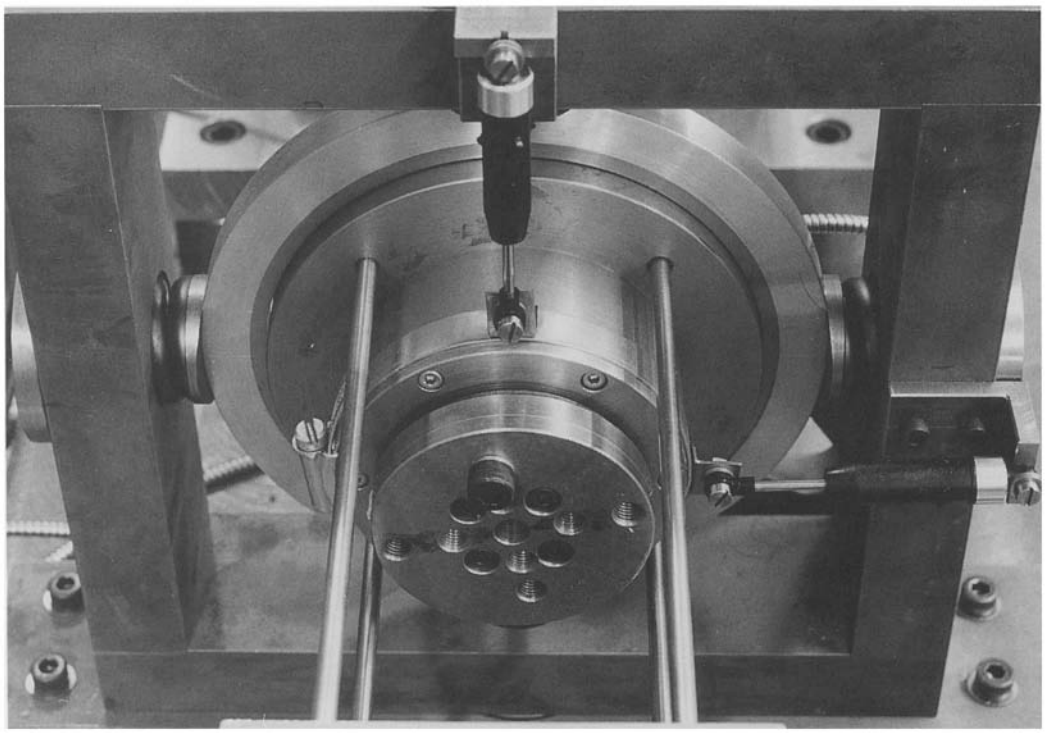

Fig. 3. Photograph of rotor and snubber ring assembly.

The rotor assembly consisted of a mild steel rotor, running in two angular contact bearings. Angular contact bearings were used so that a greater thrust capacity could be utilised, with no axial movement. Inner sleeves were fastened to the rotor to hold the bearings in place and oil seals were fitted to prevent dirt particles entering the system. Holes were drilled and tapped in both inner sleeves for the addition of imbalance weights. A pair of dampers were attached to the rotor, one in each direction, to provide the system with heavier damping. The damping is assumed to be of linear viscous type.

Four flexural rods were symmetrically clamped at one end to the outer bearing housing and at the other to a large support block. The support block was in turn bolted to a large cast iron bed. The rods were machined from a nondistorting high carbon steel to resist fatigue.

The discontinuous stiffness was provided by a ring to which four compression springs, of much greater stiffness than that of the flexural rods, were symmetrically secured. The other ends of the springs were fixed to a large frame, clamped to the bed. The ring was constructed from an aluminium ring, for lightness, since the ring is modelled as being massless, thermally shrunk onto a mild steel ring, to obtain the strength needed in the ring for impacts. The rotor ran inside the ring, with a radial clearance of 0.5 mm between the ring and the outer bearing housing, see Figures 3 and 4.

The rotor was driven by a 1.5 kW, variable speed D.C. motor, which was controlled by a single phase thyristor controller. The controller featured closed loop feedback using a tachogenerator attached to the motor, to maintain a constant speed. Utilising a Fenner-type coupling, the drive shaft of the motor was connected to a drive block, which was employed to reduce the size of the drive shaft from the motor and to mount the shaft speed monitoring

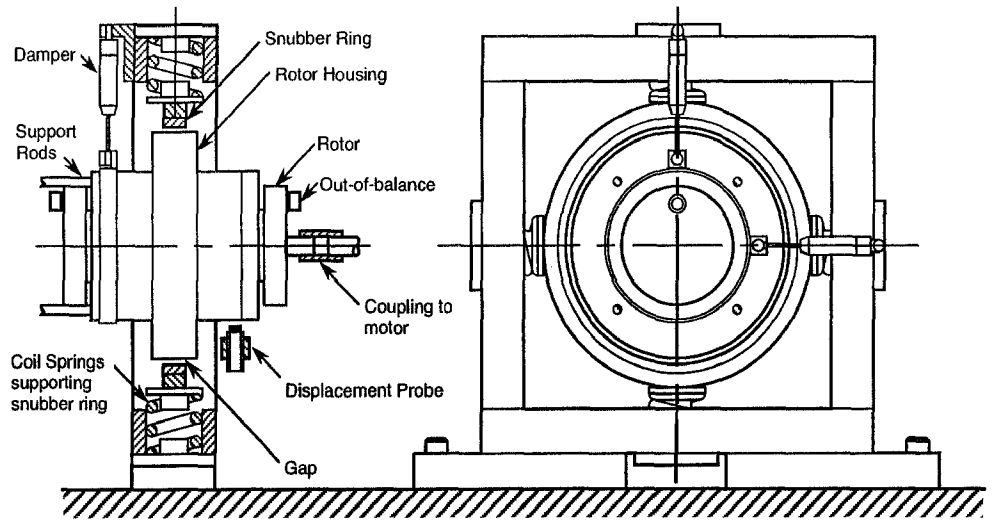

Fig. 4. Diagram of experimental set-up.

disc. Two flexible couplings were used in the connection of the drive block to a light shaft and the light shaft to the rotor and also permitted flexibility in the motion of the rotor. The shaft speed monitoring disc had a notch cut into it, which was aligned with the imbalance mass. Hence as the notch passed a light-emitting-diode optoswitch a once-per-revolution phase signal was obtained. The response of the rotor system was monitored by two noncontacting eddy probes, see Figure 5. The displacement signals from the transducer probes were filtered and differentiated. Subsequently, the displacement and velocity signals were collected by an acquisition unit, with a purpose-written program on a Hewlett Packard computer controlling the rate of sampling and the number of samples. The data was collated on the computer, where it was scaled and plotted. A flow diagram of the instrumentation used is shown in Figure 6.

4. Experimental Investigations

4.1. Experimental Procedures

The rotor was mounted in the ring so that its side was just touching the ring, hence the eccentricity of the rotor equalled the radial clearance of 0.5 mm. Only the x direction diagrams are shown in the ensuing results as the bifurcation and waterfall diagrams in both the x and y directions follow through the same type of response as the system parameter is changed. However it should be noted that, although the nature of the response is the same in both directions, the actual shape of the phase plane diagrams, Poincaré maps and spectra differ in each direction.

The shaft speed was increased from 10 to 50 Hz and the response was investigated by collecting data at 1 Hz intervals. The rotor was run at constant speed for sufficient time for it to settle into a steady state before the response was sampled. 4096 points were collected at a sampling rate of 1.3 msec for time histories and phase plane diagrams. The same number of Poincaré points were obtained using the once-per-revolution signals from the optoswitch. Waterfall plots and spectra were obtained by applying Fast Fourier Transforms to the displacement signals.

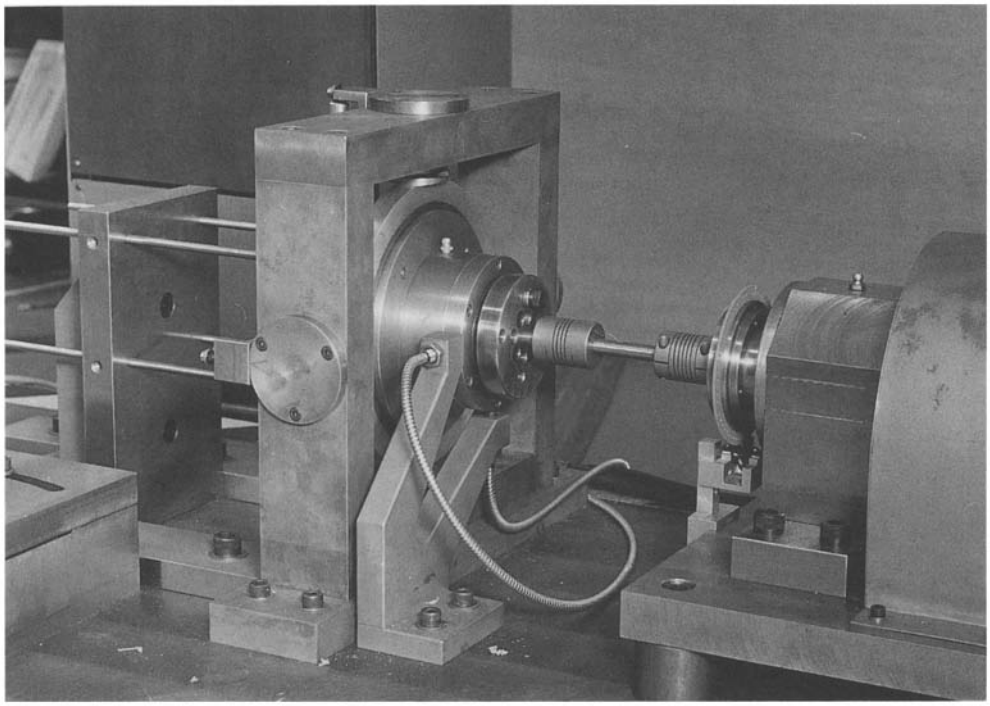

Fig. 5. Photograph of experimental rotor rig.

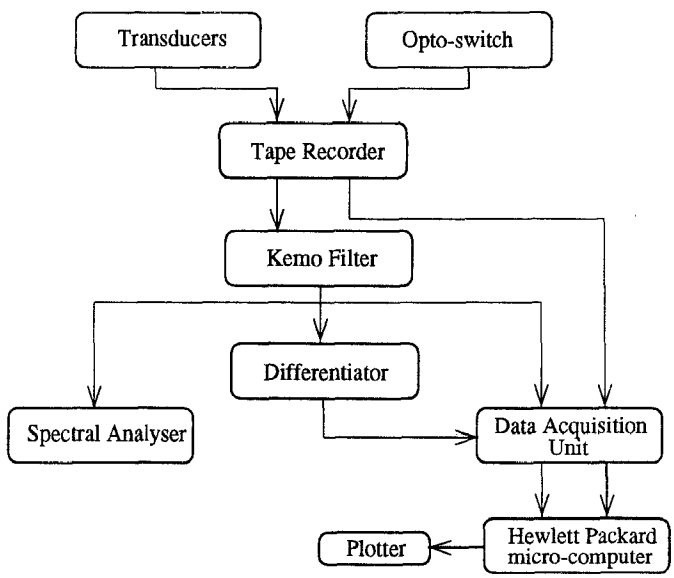

Fig. 6. Flow diagram of instrumentation.

4.2. RESULTS

The following values of the experimental parameters were chosen; a natural frequency of 15 Hz, a stiffness ratio, k_2/k_1, of 30 and a damping ratio of 0.085, measured using the

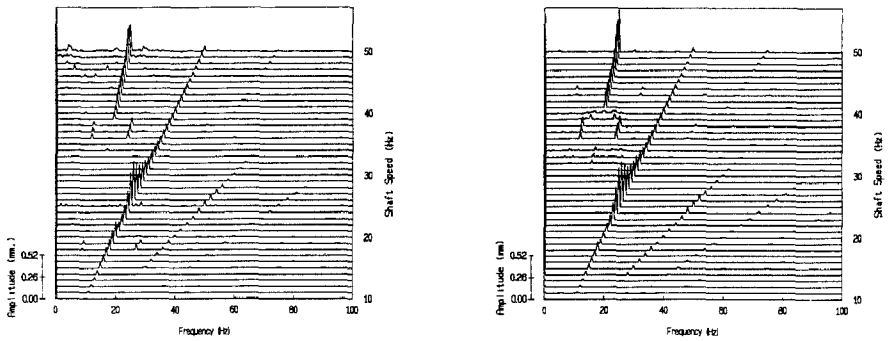

Fig. 7. (a) Experimental and (b) Theoretical waterfall plots for $\omega_n = 15$ Hz, $\hat{k} = 30$, $\nu = 0.085$, $g = \varepsilon = 0.5$ mm.

standard logarithmic decrement method. The response from the experimental rig was studied and compared with the analogous simulated response. These were obtained by increasing the shaft speed in small steps, each step starting with zero initial conditions and allowing 150.25 forcing cycles before data was sampled, in order for a steady state solution to be reached. The waterfall plot from these experimental parameters with the corresponding theoretical response are shown in Figure 7.

Comparison of the spectral content of the differently acquired responses, in Figure 7, shows a number of similarities. For increasing shaft speed the responses build up to resonance, with a peak at approximately 26 Hz ($\hat{\Omega} = 1.7$). Thereafter for both sets of results, periodic windows exist separated by broad band amplitude spectra over the same frequency ranges. Another similarity that can be clearly observed is the half subharmonic response increasing after a period three motion which occurs between 36 Hz ($\hat{\Omega} = 2.4$) and 38 Hz ($\hat{\Omega} = 2.53$).

However fewer frequency components are present in the simulated or theoretical response at the lower and higher shaft speeds; a period one motion is predominant at the lower speeds and a period two, at the higher speeds. Another distinction is the existence of a broad band of frequencies and amplitudes, between 31 and 34 Hz shaft speed, in the simulated response which is not present in the experimental results.

Figures 8 and 9 show the spatial orbits and Poincaré maps from the experimental rig and theoretical model, respectively, for periodic motion, at 36 Hz, and chaotic motion, at 39 Hz. Figure 8, for the periodic case, shows a period three motion present in the response of the rig whereas a period six motion is obtained from simulation. However, since each of the three pairs of Poincaré points in the latter diagram are situated quite close to each other it might be possible that, due to experimental noise, the Poincaré points in Figure 8 have become merged together into three points.

At 39 Hz, a ratio of $\hat{\Omega}$ of 2.6, Poincaré maps are quite similar in shape, Figure 9. The simulated maps shows a folding and stretching form. The theoretical spectrum in the waterfall plot in Figure 7 shows a broad range of frequencies, in the lower half of the spectrum, with three major spikes, one being at the forcing frequency. The other two are not a whole number fraction of the fundamental speed. The experimental spectrum shows a broad range of components at the lower frequencies, but with only two major spikes, which are the fundamental and half subharmonic components. The stretching and folding nature of the Poincaré map, together with the phase space filling traces and the wide band frequency content of the spectra all imply

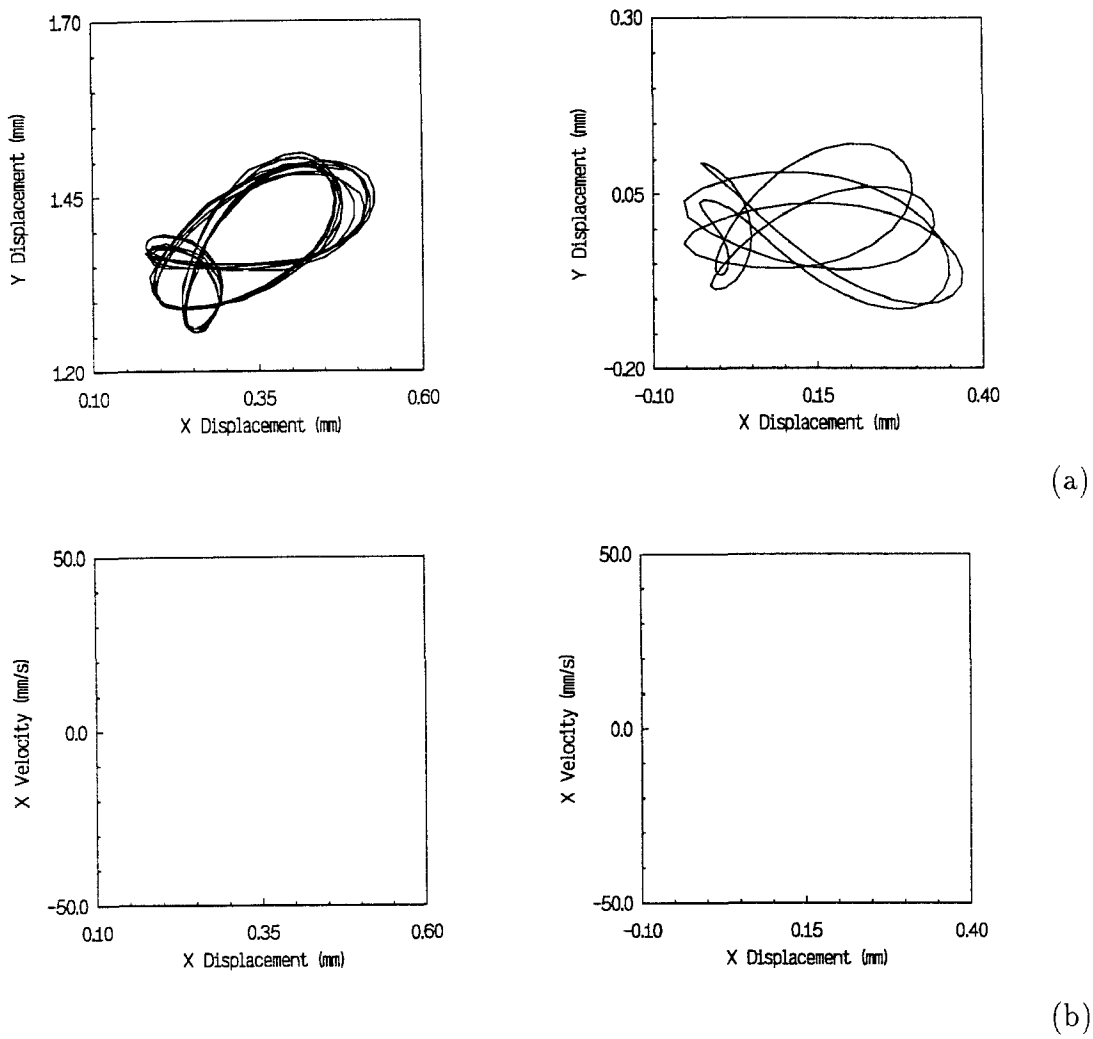

Fig. 8. (a) Spatial orbits and (b) Poincaré maps from experimental (left) and theoretical (right) investigations for $\omega_n = 15$ Hz, $\hat{k} = 30$, $\nu = 0.085$, $g = \varepsilon = 0.5$ mm, $\Omega = 36$ Hz.

chaotic motion from the simulation, although this is not so obvious from the results obtained from the rig.

Overall the results obtained from the numerical simulations were comparable with those from the experimental rig. These similarities validated the numerical model.

5. Further Numerical Investigations

As the simulated results were broadly similar to those from the experimental rig, further numerical simulations were undertaken to investigate the effect on the response of the system of systematic changes in various control parameters.

Bifurcation diagrams were used to show these effects, by plotting the amplitudes of displacement of the rotor at a phase angle of 90° of the forcing cycle, in the x direction, against the control parameter. The control parameter was increased in small steps, each step starting with zero initial conditions, except where stated otherwise, and 150.25–350.25 cycles were allowed before data was sampled, to ensure that a steady state solution had been achieved.

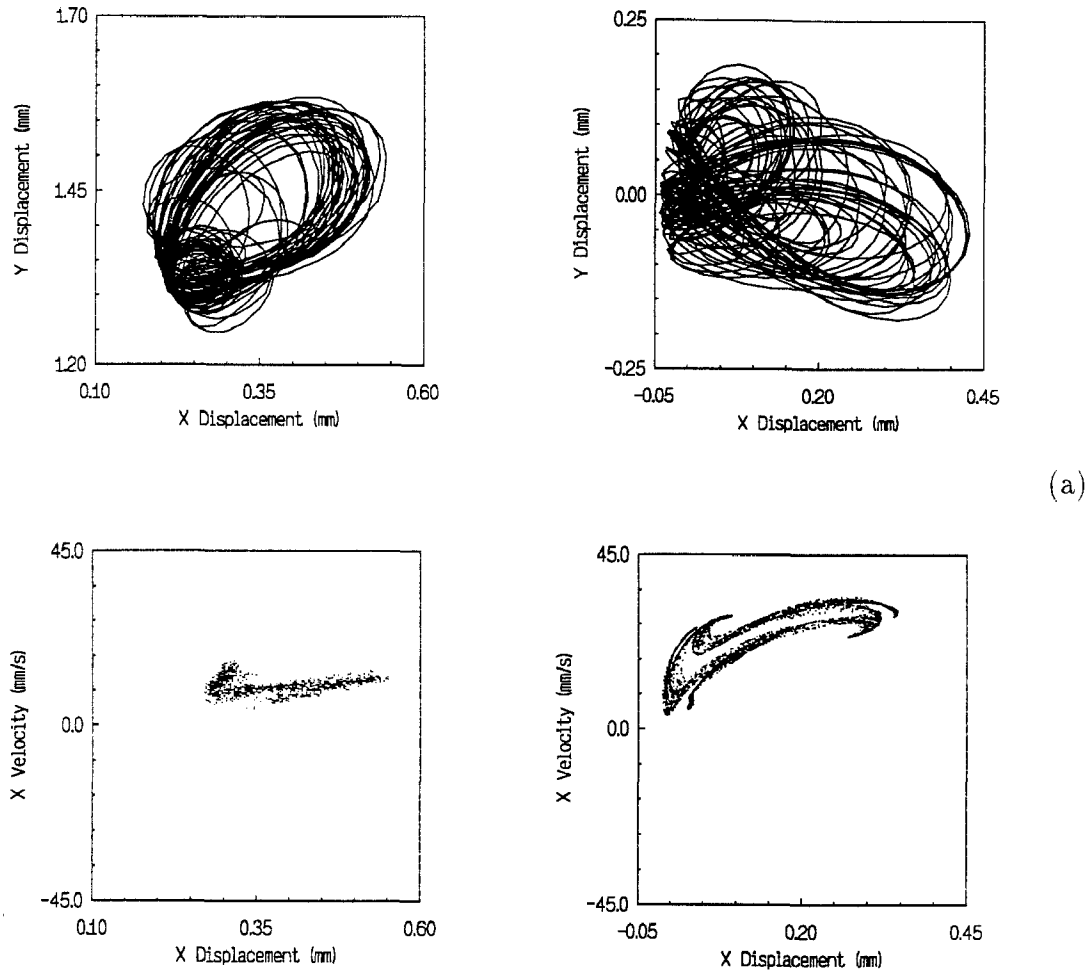

Fig. 9. (a) Spatial orbits and (b) Poincaré maps from experimental (left) and theoretical (right) investigations for $\omega_n = 15$ Hz, $\hat{k} = 30$, $\nu = 0.085$, $g = \varepsilon = 0.5$ mm, $\Omega = 39$ Hz.

The number of different points at specific values of the control parameters gives the period of the motion. When there is a dispersion of amplitudes over a range of the system parameter a quasi-periodic or chaotic response may be present.

The following sections show the change in the response of the system for varying forcing frequency, radial clearance, damping ratio and stiffness ratio respectively. In all cases the linear natural frequency of the system, ω_n remained unchanged at 15 Hz. The damping effect of the snubber ring on the rotor was not taken into account.

5.1. Variation of Forcing Frequency

The bifurcation diagrams for this section were plotted in the form of the x displacement of the rotor as a function of the frequency ratio $\hat{\Omega}$. As period one motion was found predominantly below a speed of 30 Hz in the case discussed, the frequency ratio was increased from $\hat{\Omega} = 2$ to $\hat{\Omega} = 3.25$ (30–49 Hz) in the ensuing results.

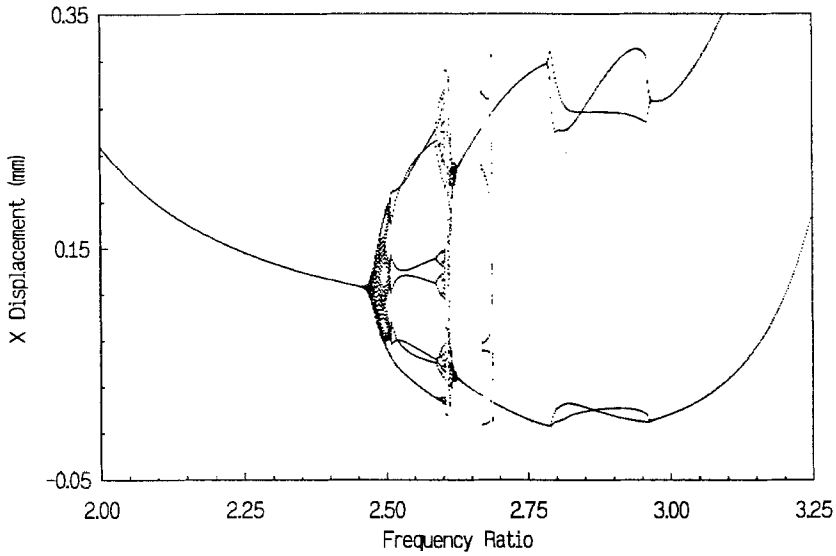

Fig. 10. Bifurcation diagram for $\hat{K} = 30$, $\nu = 0.125$, $\hat{\epsilon} = 1$, $\hat{\rho}_1 = 0.12$.

The bifurcation diagram for a stiffness ratio $\hat{K}$ of 30, a damping ratio of 0.125 and a gap and eccentricity of 0.5 mm was produced (Figure 10). These values are the same as the experimental parameters, except for an increase in the damping ratio from 0.085 to 0.125. The diagram shows a transition from period one motion into a region with dispersed points followed by a period seven motion with subsequent bifurcations through a possible band of chaos to a period two solution. This first bifurcation diagram, Figure 10, was used as a reference diagram for the production of subsequent bifurcation diagrams. The bifurcation diagrams for varying radial clearance, damping ratio, or stiffness were produced at a section through 37.4 Hz ($\hat{\Omega} = 2.49$) where a quasi-periodic motion was observed and 39 Hz ($\hat{\Omega} = 2.6$) through what appeared to be possibly a chaotic region.

The region between ratios 2.44 and 2.64 (36.6–39.6 Hz) was looked at in more detail and showed clearly the presence of a Hopf bifurcation, where the period one motion becomes quasi-periodic, present between 2.47 and 2.5 (37 and 37.5 Hz). This motion changes into a period seven followed by flip bifurcations into a broad amplitude response and a very narrow range of period five motion thereafter.

The type of motion present at any point of interest was determined using Poincaré maps. A sample of the quasi-periodic motion at $\hat{\Omega} = 2.49$) (37.4 Hz) is depicted in Figure 11, where the elliptical shape of the map and the distinct incommensurate frequencies of the spectra are characteristics of this type of motion.

The bifurcation diagram in Figure 12 shows the effect of reducing the damping ratio to a value of 0.05. The periodic and quasi-periodic responses that appeared in Figure 10 have largely disappeared and chaotic responses dominate.

5.2. Varying Damping

The amount of damping in a system can be difficult to maintain at a constant value in practice and can also drastically affect the response of the system. Hence a study of the effect of

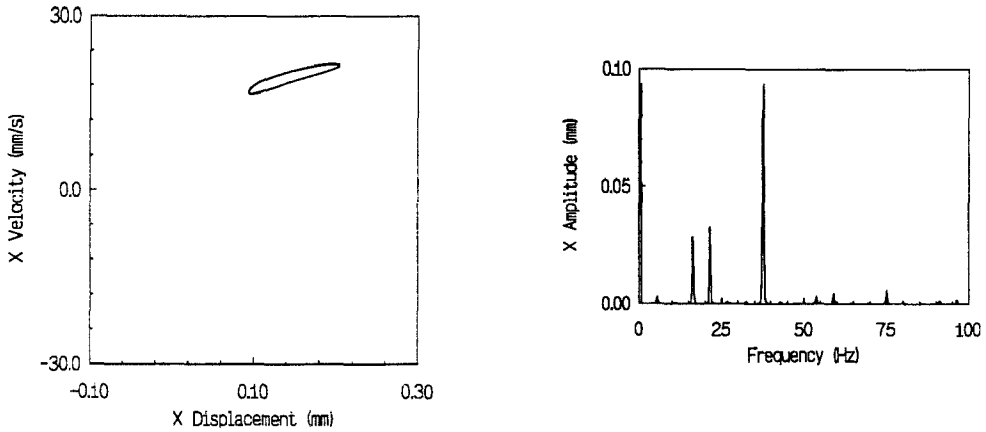

Fig. 11. Poincaré map and spectrum for $\hat{\Omega} = 2.49$, $\hat{K} = 30$, $\nu = 0.125$, $\hat{\varepsilon} = 1$, $\hat{\rho}_1 = 0.12$.

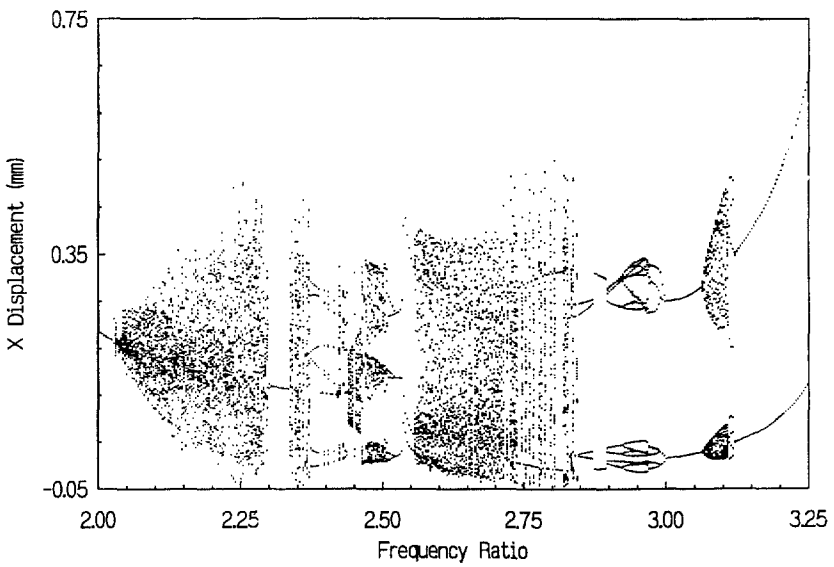

Fig. 12. Bifurcation diagram for $\hat{K} = 30$, $\nu = 0.05$, $\hat{\varepsilon} = 1$, $\hat{\rho}_1 = 0.12$.

viscous damping on the type of motion the system exhibits is shown here. The stiffness ratio, forcing speed, radial clearance and eccentricity of the rotor are kept constant.

The response of the rotor system as the damping ratio was varied at a frequency ratio of 2.49 is depicted in the bifurcation diagram in Figure 13. A three-band response exists until periodic motion is reached at about ν equal to 0.107. This subsequently changes into a quasi-periodic motion, before the response gradually becomes a period one motion.

Figure 14, for a frequency ratio, $\hat{\Omega}$ of 2.6, shows a wide amplitude response at lower levels of damping, from 0.08 to about 0.115, after which the motion takes on a periodic form, through what appears to be a period halving route. Further increase in the damping ratio leads to period doublings into a wide-band response. From this scatter of amplitudes a period seven motion appears over a very small range of damping ratio (0.131–0.132). This subsequently changes into a period two motion.

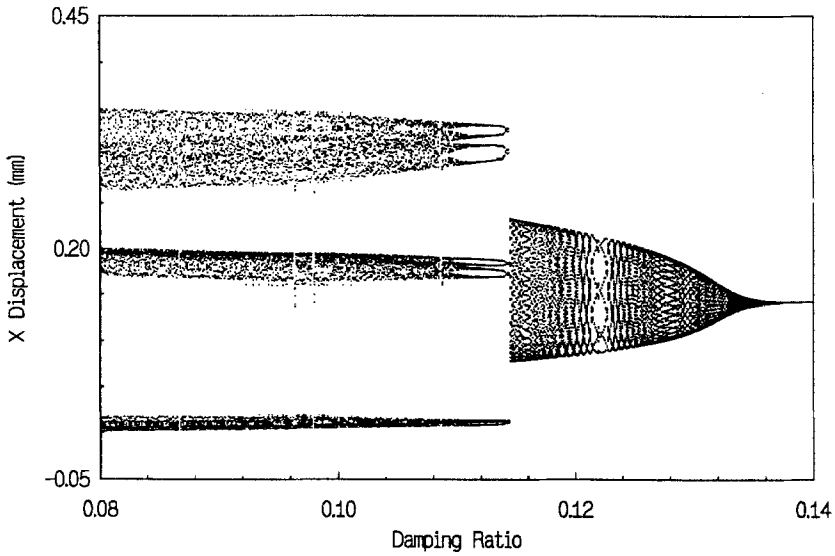

Fig. 13. Bifurcation diagram for $\hat{\Omega} = 2.49$, $\hat{K} = 30$, $\hat{\varepsilon} = 1$, $\hat{\rho}_1 = 0.12$.

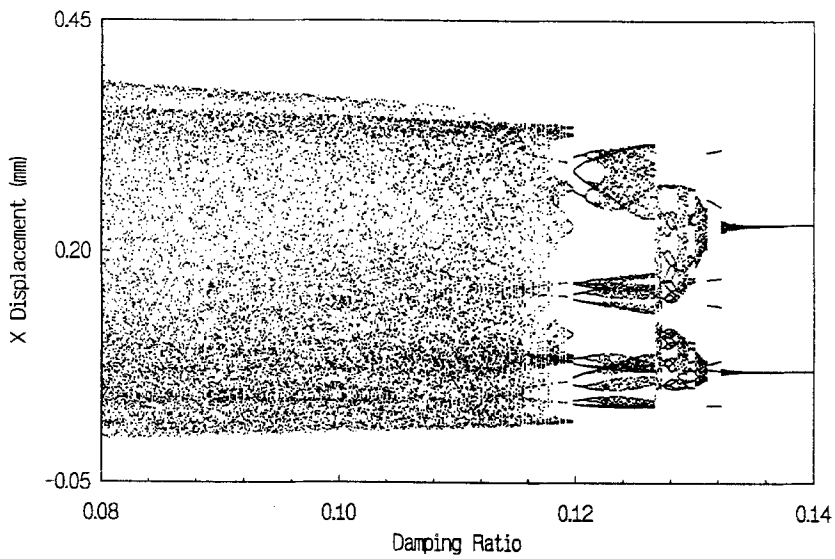

Fig. 14. Bifurcation diagram for $\hat{\Omega} = 2.6$, $\hat{K} = 30$, $\hat{\varepsilon} = 1$, $\hat{\rho}_1 = 0.12$.

5.3. Varying Clearance

The radial clearance between the rotor and the snubber ring plays an important part in the behaviour of the system in that it can stipulate the amount of 'rattle' of the rotor in the bearing clearance.

Here the radial clearance, g is slowly increased, with the eccentricity of the rotor, ε, equal to g when the rotor is at rest. Thus the dimensionless parameter $\hat{\rho}_1$ slowly decreases in this analysis. In this section the bifurcation diagrams are plots of the x displacement against the radial clearance, where the stiffness and damping ratios were 30 and 0.125 respectively.

Increasing the radial clearance from 0.1 to 0.7 mm with a constant shaft speed ratio of 2.49 at first and then 2.6, gives the response shown in Figures 15 and 16, respectively. Figure 15

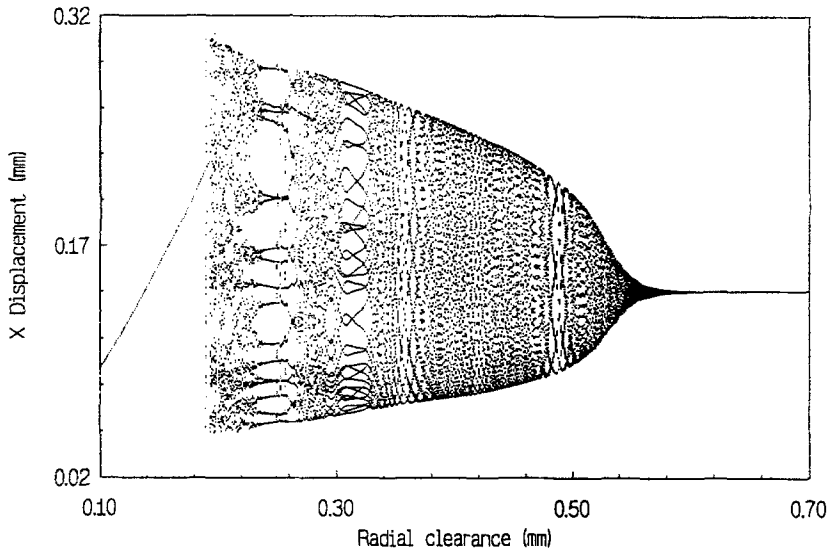

Fig. 15. Bifurcation diagram for $\hat{\Omega} = 2.49$, $\hat{K} = 30$, $\nu = 0.125$, $\hat{\varepsilon} = 1$.

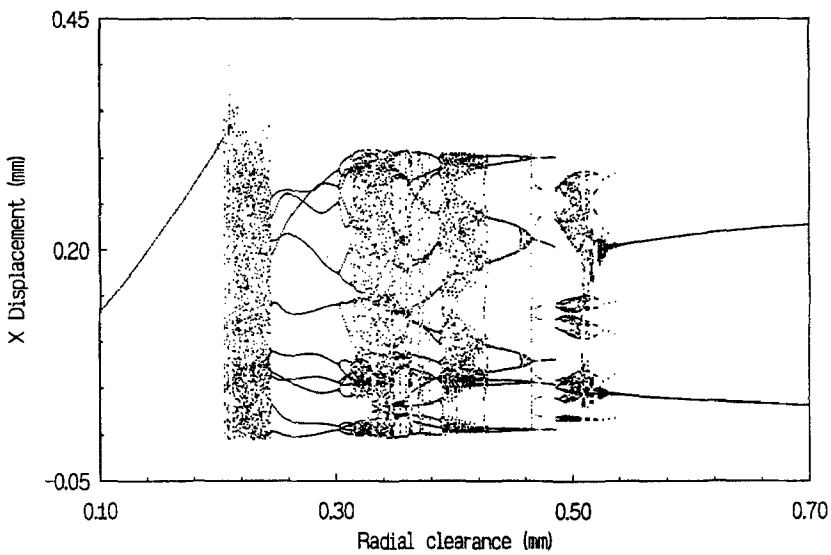

Fig. 16. Bifurcation diagram for $\hat{\Omega} = 2.6$, $\hat{K} = 30$, $\nu = 0.125$, $\hat{\varepsilon} = 1$.

corresponds to a section through the bifurcation diagram in Figure 10 where quasi-periodic motion existed for $g = \varepsilon = 0.5$ mm, at $\hat{\Omega}$ equal to 2.49. The response in this case is principally quasi-periodic. In Figure 16, corresponding to a section through Figure 10, at a ratio of $\hat{\Omega}$ of 2.6, the response is notably different from that in the preceding diagram, being mainly periodic, interspersed with wide-band responses.

In both diagrams the amplitude of the period 1 motion increases to a critical value prior to a sudden jump into a wide band response. This jump was investigated by further bifurcation diagrams, which showed no evidence of period doubling occurring. In the case of Figure 15 the response reaches a quasi-periodic motion having passed through high order subharmonic

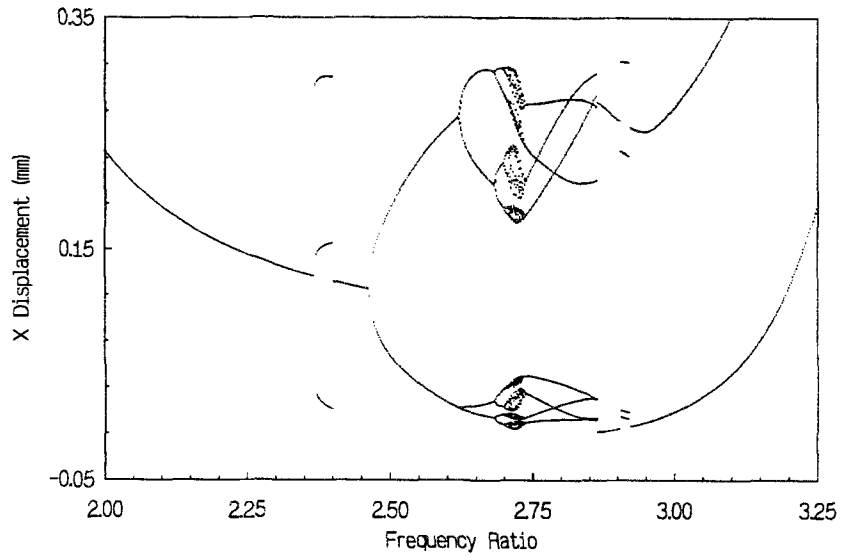

Fig. 17. Bifurcation diagram for $\hat{K} = 30$, $\nu = 0.125$, $\hat{\varepsilon} = 1$, $\hat{\rho}_1 = 6.1 \times 10^{-6}$ in x direction.

windows separated by a quasi-periodic band. This motion gradually reverts into a constant amplitude, period one response as the radial clearance is enlarged further.

The bifurcation diagram in Figure 16 shows that a further increase in radial clearance causes the onset of subharmonic motions of various orders, interspersed with chaotic bands. The response eventually becomes a half subharmonic motion.

A decrease in the damping ratio from 0.125 to 0.05 causes the quasi-periodic responses seen in Figure 15 to disappear and produces a largely chaotic response. This observation agrees with the results shown in the bifurcation diagram in Figure 13 and suggests that for quasi-periodic responses to occur there must not only be cross-coupling between the x and y directions, but also a substantial amount of damping.

The value of gap, g, and eccentricity, ε, were then set to 100 m, ($\hat{\rho}_1 = 6.1 \times 10^{-6}$) to simulate a discontinuity confined to motion in the x direction as a result of the rotor coming into contact with a more or less flat surface and only contacting the snubber springs on one side. This particular situation has also been modelled in the past by Ehrich [7, 14] and Kim and Noah [6]. Both the x and y direction bifurcation diagrams are produced here, Figures 17 and 18 respectively, to show the uncoupled response of the system in the two directions.

The period doubling route through flip bifurcations is clearly evident in Figure 17. A period one response jumps into a period three motion as the forcing frequency is increased. This period three coexists with the period one motion over a narrow frequency range, before returning to a response that solely consists of the period one motion. Flip bifurcations then occur which lead to a four band attractor, after which the motion reverts back to periodic motion, primarily through a period halving route. This bifurcation diagram shows some resemblance to the bifurcation diagram produced from a single degree of freedom model. This is a result of the rotor system behaving like a single degree of freedom system in the x direction due to the decoupling of the x and y motions as a result of the large radial clearance.

Figure 18, the y direction bifurcation diagram, shows a linear response. Further investigation revealed that the y response starts behaving differently from that of the x direction at a

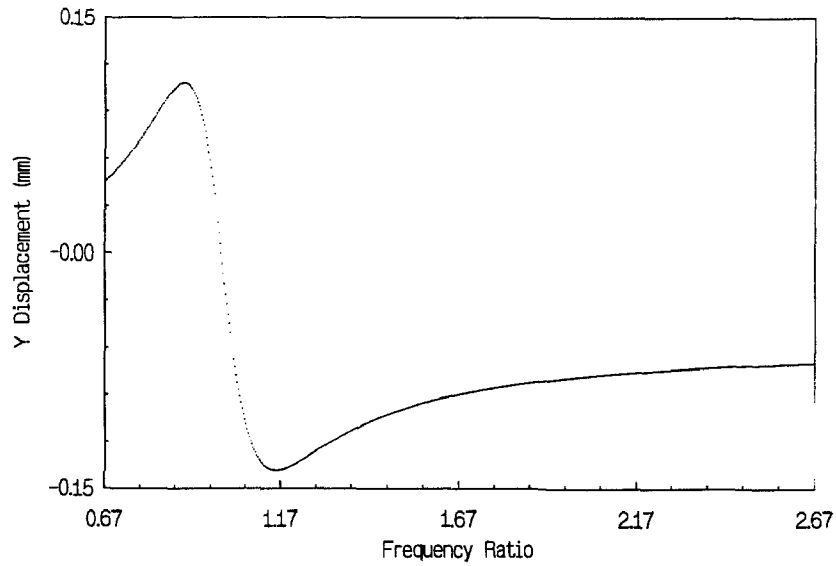

Fig. 18. Bifurcation diagram for $\hat{K} = 30$, $\nu = 0.125$, $\hat{\varepsilon} = 1$, $\hat{\rho}_1 = 6.1 \times 10^{-6}$ in y direction.

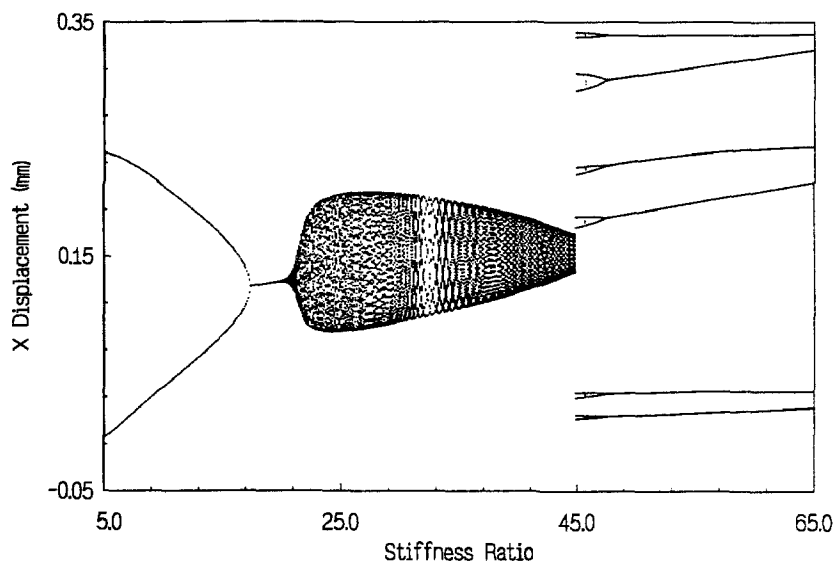

Fig. 19. Bifurcation diagram for $\hat{\Omega} = 2.49$, $\nu = 0.125$, $\hat{\varepsilon} = 1$, $\hat{\rho}_1 = 0.12$.

radial clearance of about 5 cm (that is $\rho_1 = 0.0012$), but the value of g at which the y response becomes effectively linear in nature was found to be at about 25 cm (that is $\rho_1 = 0.003$).

5.4. Varying Stiffness Ratio

In most of the previous studies, the investigators looked at the limiting case of an impact situation where an infinite stiffness ratio was utilised [1, 15–17]. However, in real systems there is always a finite stiffness. Here the effect of increasing the stiffness ratio, from 5 to 65, is investigated and shown in Figure 19, where the speed ratio, $\hat{\Omega}$ is 2.49, the damping ratio is 0.125 and the radial clearance and eccentricity are 0.5 mm.

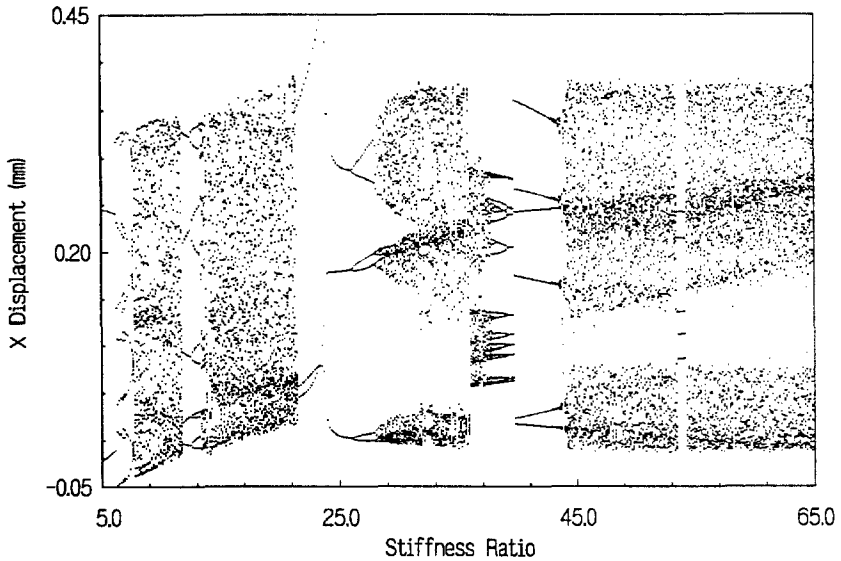

Fig. 20. Bifurcation diagram for $\hat{\Omega} = 2.49$, $\nu = 0.05$, $\hat{\varepsilon} = 1$, $\hat{\rho}_1 = 0.12$.

At a stiffness ratio of 5, a period two motion exists at first, which gradually converges into a period one response. This leads to a quasi-periodic motion which slowly reduces in amplitude and then suddenly jumps to a periodic motion of order 12 and then 6, as the stiffness ratio is increased further. The response remains periodic for larger stiffness ratios.

Increasing the stiffness ratio, $\hat{K}$ causes an increase in the degree of nonlinearity in the system, which does not necessarily produce chaotic responses, but may also produce either periodic or quasi-periodic responses.

Decreasing the damping ratio from 0.125 to 0.05 once again causes the quasi-periodic responses to disappear, with the response becoming mainly chaotic again, as shown in Figure 20.

The bifurcation diagram produced for a forcing speed ratio of 2.6 (39 Hz), Figure 21, shows an initial period two motion, as for the previous case, but over a larger stiffness ratio range. The subharmonic motion abruptly changes into a wide-band regime, followed by a sequence of period halvings into subharmonic motions of various orders. A reversal back into a chaotic regime subsequently takes place, which exists for larger stiffness ratios.

6. Discussion

In general, an increase in damping or imbalance (or decrease in radial clearance) in the system appears to eventually reduce response to periodic form. However, the results for increasing the degree of nonlinearity (that is, the stiffness ratio) did not appear to show any particular trend, although at lower stiffness ratios only periodic responses resulted. These observations may be useful in choosing the technique to solve the equations of motion of the particular system under investigation. For example, if a weakly nonlinear system is being studied with heavily damped levels or large clearance to imbalance ratios, an harmonic balance technique, as used by [6, 18, 19], may be employed in finding all possible solutions.

Cross-coupling between motions in the x and y directions with a substantial amount of damping appears to be necessary for quasi-periodic motions to occur. This agrees with the

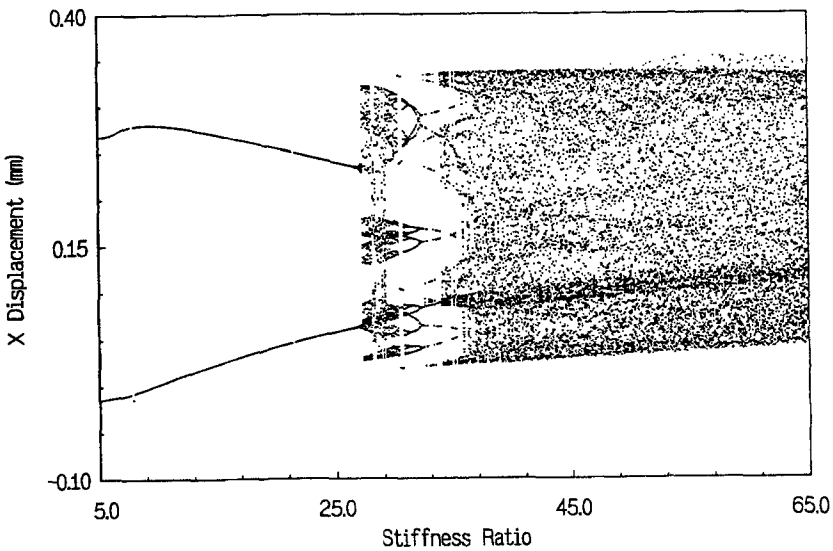

Fig. 21. Bifurcation diagram for $\hat{\Omega} = 2.6$, $\nu = 0.125$, $\hat{\varepsilon} = 1$, $\hat{\rho}_1 = 0.12$.

work of Kim and Noah [6]. In their study, however, they found it necessary to include a cross-coupling stiffness term in their equations of motion of a Jeffcott rotor, which was mounted asymmetrically in a large bearing clearance, in order to obtain a quasi-periodic response. In this study, the small radial clearances present in the system induce cross-coupling effects. Ehrich [14] has also studied a similar rotor system, but did not appear to obtain quasi-periodic responses as the model considered again took the radial clearance to be very large compared to the orbit of the rotor.

For large clearances, with the rotor placed eccentrically against the snubber ring in one direction, the nature of the response in each direction depends on the coordinate system used during measurement. When the response monitoring devices are placed in line with the principal axes of the eccentricity, a linear response may be seen in one direction and a nonlinear in the other. However if the devices are placed at some angle α to the eccentricity, both responses will generally appear to be nonlinear. This may be explained by the transformation:

$$x' = x\cos\alpha + y\sin\alpha$$

$$y' = y\cos\alpha - x\sin\alpha,$$

where x and y are the principle axes of the eccentricity and x' and y' are the axes along which the transducers are placed. If $x(t)$ is nonperiodic, $y(t)$ periodic and $\alpha \neq n\frac{\pi}{2}$, where $n = 0, \ldots, \infty$, then $x'(t)$ and $y'(t)$ will be nonperiodic.

Ehrich [14] reported the production of an elongated chaotic orbit from this rotor model, operating between 8 and 9 times its fundamental frequency, but a more circular orbit from an experimental test on a high speed gas turbine rotor. This discrepancy was explained as being due to both a time shift between the two signals from the transducers', and measurement along nonprincipal axes of the eccentricity. The numerically-obtained orbit, which is effectively decoupled in the x and y directions due to the large clearance, is likely to be more elongated than that from the experimental tests. Simulations of the system considered here, however, suggest that such orbits may also be exhibited if there is coupling between the motions due to the curvature of the clearance. This is substantiated by the orbits produced in Figure 22 for

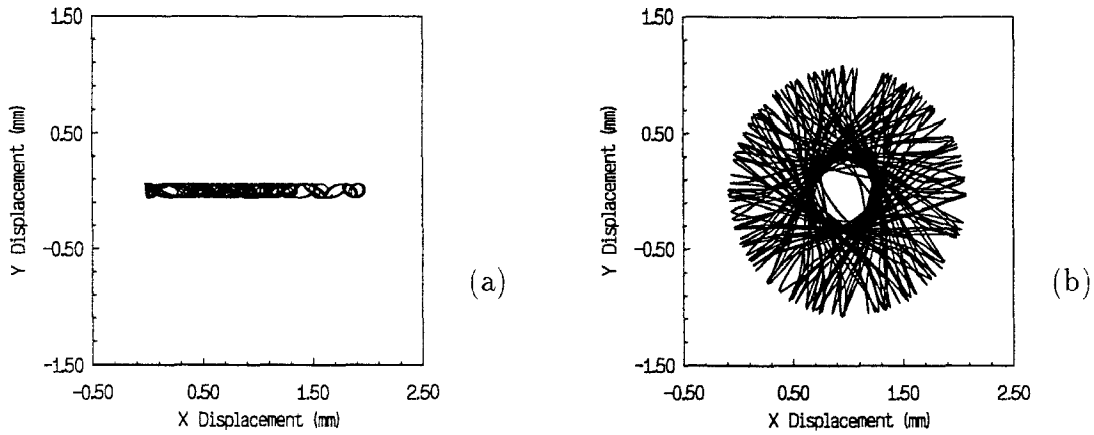

Fig. 22. Spatial orbits for zero initial conditions and (a) $g = \varepsilon = 10$ m, (b) $g = \varepsilon = 1$ mm.

shaft speeds of 8.57 times that of the bilinear natural frequency of the system and a stiffness ratio, $\hat{K}$ of 3000. The speed ratio used is that used by Ehrich for his simulations. The orbit in Figure 22(a) shows that for large clearance to orbit ratios the rotor does not contact the opposite side of the snubber ring and an elongated orbit results. The motion in the y direction is linear while that in the x is chaotic. However for small clearance to orbit ratios, a circular chaotic orbit results, Figure 22(b), as the rotor now both makes contact with the opposite side of the ring and the motions are coupled by the geometry. Both simulations were started with zero initial conditions. For some cases quasi-periodic responses, with a circular envelope of the orbit, and elongated chaotic responses were found to coexist.

Fatigue analysis performed on the time histories from the primary supports' response of the rotor model and a single degree of freedom model, through a series of bifurcations, suggested that the subharmonic motions were more damaging than the chaotic motions, which were in turn more damaging than the simple fundamental responses. This is supported by the time histories of the respective motions, which show that the amplitudes of the fundamental responses tend to be smaller than those of the chaotic responses, which in turn are smaller than those of the subharmonic motions.

7. Conclusions

Similarity in the responses from an experimental rig and numerical simulations, for relatively large values of damping was obtained, thus supporting the validity of the theoretical model for realistic damping levels.

From both experimental and numerical results, it has been observed that a wide variety of motions can be exhibited by this system, from periodic to quasi-periodic to chaotic. Overall, the results from the numerical model predict that chaotic motions can exist over a large areas of the parameter space.

A major conclusion drawn from the results of the numerical model is that the response of this system is extremely sensitive to changes in the system parameters. Small changes in these parameters can convert the response from being periodic to quasi-periodic or chaotic and vice versa. These characteristics can make condition monitoring difficult, although for constant system parameters; excitation frequency, imbalance, stiffness ratio and damping ratio, a value of radial clearance (with the eccentricity equal to the radial clearance) exists for which the

responses in the x and y directions are dissimilar. Beyond this, there exists a larger value of clearance for which the responses in the two directions become uncoupled, which results in the y direction response behaving linearly.

Another outcome is that cross-coupling between motions in the x and y directions appears to be necessary for quasi-periodic motions to occur.

Acknowledgements

The authors wish to acknowledge the financial assistance provided by the Science and Engineering Research Council under grant GR/F29158.

References

1. Shaw, S. W. and Holmes, P. J., 'A periodically forced piecewise linear oscillator', *Journal of Sound and Vibration* **90**(1), 1983, 129–155.
2. Mahfouz, I. A. and Badrakhan, F., 'Chaotic behaviour of some piecewise linear systems', Parts I and II, *Journal of Sound and Vibration* **143**(2), 1990, 255–288.
3. Akay, A., Rhee, J., and Wu, X., 'Chaotic response of a dynamic system with a clearance', in *Proceedings of the Eight World Congress on the Theory of Machines and Mechanisms*, Prague Czechoslovakia, August 26–31, 1991, pp. 343–345.
4. Wiercigroch, M., Neilson, R. D., and Gonsalves, D. H., 'Chaos occurring in systems with discontinuities', in *Proceedings of the AMSE Conference on Signals and Systems*, Warsaw, Poland, July 15–17, 1991, pp. 129–138.
5. Pfeiffer, F. and Kunert, A., 'Rattling models from deterministic to stochastic processes', *Nonlinear Dynamics* **1**, 1990, 63–74.
6. Kim, Y. B. and Noah, S. T., 'Bifurcation analysis for a modified Jeffcott rotor with bearing clearance', *Nonlinear Dynamics* **1**, 1990, 221–241.
7. Ehrich, F. F., 'High order subharmonic response of high speed rotors in bearing clearance', *ASME Journal of Vibration, Acoustics, Stress and Reliability in Design* **110**, 1988, 9–16.
8. Neilson, R. D. and Barr, A. D. S., 'Dynamics of a rigid rotor mounted on discontinuously nonlinear elastic supports', *Proceedings of the I. Mech. E.* **202**(C5), 1988, 369–376.
9. Neilson, R. D. and Barr, A. D. S., 'Response of two elastically supported rigid rotors sharing a common discontinuously nonlinear support', in *Proceedings of the I. Mech E 4th International Conference on Vibrations in Rotating Machinery*, Heriot-Watt University, Scotland, September 13–15, 1988, pp. 589–598.
10. Nayfeh, A. H., *Introduction to Perturbation Techniques*, Wiley, New York, 1981.
11. Borthwick, W. K. D., 'The numerical solution of discontinuous structural systems', in *Proceedings of the 2nd International Conference on Recent Advances in Structural Dynamics*, University of Southampton, England, April 9–13, 1984, pp. 307–316.
12. Neilson, R. D., 'Dynamics of simple rotor systems having motion dependent discontinuities', PhD Thesis, University of Dundee, 1988.
13. Neilson, R. D. and Gonsalves, D. H., *Chaotic Motion of a Rotor System with a Bearing Clearance*, in Applications of Fractals and Chaos, Springer-Verlag, Berlin 1993.
14. Ehrich, F. F., 'Some observations of chaotic vibration phenomena in high speed rotordynamics', *Journal of Vibration and Acoustics* **113**, 1991, 50–57.
15. Thompson, J. M. T. and Stewart, H. B., *Nonlinear Dynamics and Chaos*, Wiley, Chichester, 1986.
16. Shaw, S. W. and Holmes, P. J., 'A periodically forced impact oscillator with large dissipation', *Journal of Applied Mechanics* **50**, 1983, 849–857.
17. Nguyen, D. T., Noah, S. T., and Kettleborough, C. F., 'Impact behaviour of an oscillator with limiting stops', Parts I and II, *Journal of Sound and Vibration* **109**(2), 1986, 293–325.
18. Choi, Y. S. and Noah, S. T., 'Nonlinear steady-state response of a rotor support system', *ASME Journal of Vibration, Acoustics, Stress and Reliability in Design* **109**, 1987, 255–261.
19. Choi, Y. S. and Noah, S. T., 'Forced periodic vibration of unsymmetric piecewise-linear systems', *Journal of Sound and Vibration* **121**(1), 1988, 117–126.